LASTA 2.0: Validation of a Reverse Time Integration Method

Joseph Steer*, Justin Clarke†, Matthew McGilvray ‡, and Luca Di Mare §
Oxford Thermofluids Institute, University of Oxford, Oxford, UK

Shock tube experiments provide critical insight into the thermochemical processes that occur in the shock layer of hypersonic flight vehicles and are used to validate many chemical-kinetic and radiative models for vehicle design. Shock tube flows exhibit a number of non-ideal behaviours that must be accounted for when interpreting experimental data. Previous work has shown that variations in shock speed and boundary layer growth along the length of the shock tube have a strong effect on the test slug properties. The LAgrangian Shock Tube Analysis code (LASTA) is an a posteriori tool that successfully addressed this problem, allowing reconstruction of the test slug from an experimentally obtained shock trajectory. LASTA 2.0 is presented here, which further constrains the test slug properties using an additional experimental pressure boundary condition whose effects are included via a backwards time integration scheme. The tool is validated against ideal gas cases following accelerating and decelerating shock trajectories, each with a tube-end Mach number of 6.5 and a fill pressure of 66.66 Pa. Agreement between the method and results from a viscous, axisymmetric Navier-Stokes solution is found to be within 1% in pressure and temperature in the majority of cases. Improved agreement with experimental data is evident when compared to the previous version of LASTA, particularly where there is strong shock speed non-uniformity.

Nomenclature

a	=	Speed of sound, $\mathrm{m\,s^{-1}}$
β	=	Shape factor, -
Λ	=	Shock speed, $\mathrm{m\,s^{-1}}$
d	=	Tube diameter, m
e	=	Internal energy, J
γ	=	Ratio of specific heats, -
h	=	Enthalpy, $\mathrm{MJ\,kg^{-1}}$
ℓ	=	Test slug length, m
m	=	Mass, kg
η	=	Non-dimensional post-shock distance, -
ρ	=	Density, $\mathrm{kg\,m^{-3}}$
p	=	Pressure, Pa
r	=	Tube radius, m
S	=	Core flow effective diameter, m
t	=	Time, s
τ	=	Test time, µs
u	=	Velocity, $\mathrm{m\,s^{-1}}$
υ	=	Radial velocity, $\mathrm{m\,s^{-1}}$
μ	=	Viscosity, Pa s
x	=	Distance from primary diaphragm, m
χ	=	Distance behind the shock, m
w	=	Characteristic variable

*DPhil Candidate, Oxford Thermofluids Institute, University of Oxford
†DPhil Candidate, Oxford Thermofluids Institute, University of Oxford
‡Professor, Oxford Thermofluids Institute, University of Oxford, AIAA Member.
§Associate Professor, Oxford Thermofluids Institute, University of Oxford, AIAA Member.

I. Introduction

Shock tubes are currently one of the best available platforms for shock layer radiation measurements because of their relative simplicity and versatility. A shock tube experiment aims to match gas composition, density, and shock speed, thereby obtaining direct similarity between the flight stagnation line and the shock tube flow. Shock tube flows are considered 'chemically clean' meaning that the test gas is chemically undisturbed before the experiment takes place. This offers a significant advantage over other experimental facilities and makes shock tubes highly informative for the investigation of non-equilibrium chemical kinetics. Figure 1 shows a distance-time plot of the typical wave processes occurring in a generic shock tube during a test. Initially, the test gas, matching the density and composition of the free stream flight condition of interest, resides in the region denoted 'Shock Tube'. The high pressure driver gas ruptures the primary diaphragm and drives a strong shock wave through the test gas. To obtain similarity with flight, the shock speed should match the flight case. The region of useful test gas, denoted τ, grows until it reaches a maximum value governed by the boundary layer growth [1]. Measurements of radiation behind the shock wave can be made at any point along the length of the shock tube, but they are typically obtained at a measurement window located at the downstream end of the facility where the test time is maximised [2, 3]

Despite their ostensibly simple operation, several subtle complexities inherent in shock tubes conspire to make accurate a priori simulations difficult, among these is non-uniformity of the shock speed as it propagates through the tube. This non-uniformity is caused by interaction between the shock wave and complex compression and expansion waves which arise from a variety of sources. One source is the growth of the boundary layer in the test slug and driver gas, which serves to attenuate the shock by entraining mass from the core flow [1, 4]. The motion of the contact surface, the interface between the expanded driver gas and test gas, also produces waves which affect the shock speed [5]. The behaviour of the contact surface is itself dependent on many factors including the driver technology employed, the driver condition chosen for the experiment, and the primary diaphragm rupture behaviour [6]. Additionally, the non-equilibrium thermochemistry taking place in the shock layer is also seen to affect the shock speed [7, 8].

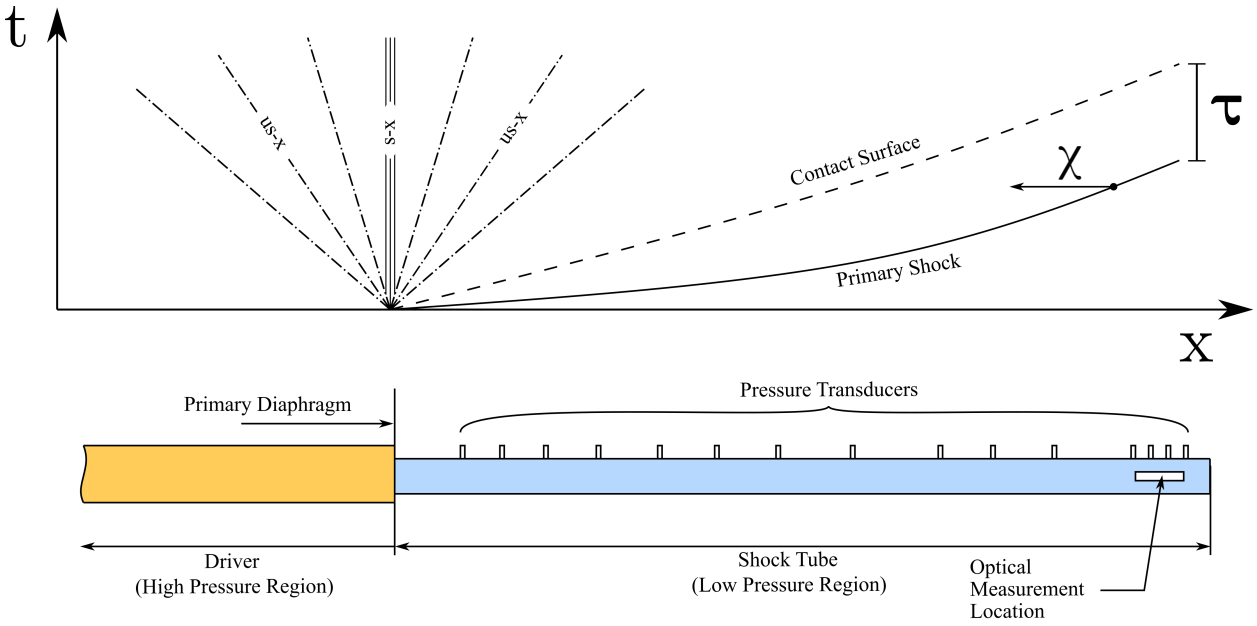

Fig. 1 Position-time diagram of wave processes in a generic shock tube, adapted from Collen [3]

A variety of approaches have been taken to model shock tube flows, a summary of the key features of several is include in Table 1. Perhaps the simplest approach is state-to-state or 0D modelling. These codes use a minimum number of inputs, for example initial pressure and shock speed, and make an ideal gas or equilibrium assumption to define the full flow properties. One of the earliest examples of these codes is the Equilibrium Shock Tube Conditions (ESTC) code which was later re-implemented in ESTCj [9]. This code utilises CEA [10] for thermochemical properties and allows modelling of many simple flow processes found in pulse facilities including normal shocks, oblique shocks, steady and unsteady expansions. The capabilities of ESTCj form the basis for PITOT [11], which is intended as a 'virtual facility' state-to-state code to allow rapid flow condition development. PITOT began as an equilibrium gas expansion

tube solver but it now allows modelling of many types of facilities including shock tubes/tunnels and reflected shock tunnels. State-to-state solvers are convenient for simple calculations but by definition cannot and are not intended to account for additional complexities arising in impulse facilities. For example, state-to-state solvers assume constant shock speed in all processes, which is not the case in reality.

1D models offer improved resolution of the test slug properties at a higher computational cost. L1d [12], a quasi-one-dimensional Lagrangian CFD code designed to simulate free-piston driven impulse facilities, is one such example. This code simulates transient flow processes in the facility including piston dynamics. Gas slugs along the length of the tube are discretized axially into fixed mass 'slices' whose properties are tracked over the course of the simulation. Heat transfer and friction are modelled at the tubes walls, although the boundary layer is not simulated explicitly. L1d may be tuned to match experimental results, for example static pressure traces, by variation of one or more loss factors which account for non-ideal processes such as primary diaphragm rupture and flow through the orifice constriction between the driver and driven tubes. This approach has proved successful in many cases, examples include McGilvray et al. [13], Gildfind et al. [14], however difficulty has been encountered in accurately matching properties at the acceleration tube exit which has been attributed to an inability to account for the effects of shock attenuation.

Full facility, 2D axisymmetric and 3D simulations offer the highest fidelity models of impulse facilities. Many codes with these capabilities are in use, such as Eilmer 4 [15] and US3D [16]. In general terms, these codes solve compressible Navier-Stokes equations over the flow domain subject to customizable user defined boundary conditions. Many turbulence models, reaction schemes, grid structures, and numerical methods are at the disposal of the user. Excellent agreement is obtained between experiment and simulation for a wide variety of test cases with such codes and they are an indispensable tool in hypersonics research, particularly for interplanetary vehicle design. Despite these advantages, like the other methods mentioned, these codes struggle to predict shock speed non-uniformity in impulse facilities.

Several codes have been developed specifically to address modelling of the thermochemical non-equilibrium in shock tubes. Such codes typically solve one dimensional Navier-Stokes equations coupled to a finite rate chemistry model with the immediate post-shock, frozen gas state as a boundary condition. The gas is then allowed to thermochemically relax to an equilibrium state over a time governed by the chemistry model utilised. The POst SHock relAXation solver or POSHAX [17, 18] solves for post-shock thermochemistry subject to a Rankine-Hugoniot assumption or constant post shock velocity. This tool has been used by a variety of sources to analyse experimental results [19–21], however boundary layer growth in shock tubes is seen to strongly affect the post shock velocity profile which limits the applicability of the code to experimental cases [22]. The approach of relaxing the gas from a predetermined post shock state also neglects the effects of diffusion and does not allow the user to resolve the shock structure. The Non-Equilibrium Shock Solver (NESS) is a similar tool models the shock tube in cylindrical coordinates and solves the two-dimensional, two-temperature Navier-Stokes equations to resolve the post shock state. This approach allows the shock structure to be resolved and direct comparison to experiment is possible by implementation of a radial source term that mimics mass removal by the boundary layer. By variation of the radial velocity source term, the code may be applied to other geometries, such as the stagnation line of a blunt body with the correct particle time of flight achieved. In the shock tube case, NESS operates under the assumption of constant shock speed, which means that in cases of strong shock speed non-uniformity its predictions are likely to deviate from experiment.

Variation in shock speed can have a significant effect on the observed experimental spectra. Collen et al. [21] shows that for two test with the same shock speed at the measurement window, the post-shock Oxygen 777 nm equilibrium radiance can vary by over 100 %. This effect has been shown to be present irrespective of the experimental facility or driver technology employed, having been observed and quantified in results from the EAST [23] and T6 [21] facilities. Satchell et al. [24, 25] developed a model known as LASTA specifically to account for shock speed non-uniformities in shock tube flows. LASTA predictions show excellent agreement with experimental data and confirm the importance of shock speed variation in shock tube experiments. LASTA presently solves coupled mass and energy conservation equations for each lagrange, however conservation of momentum is never ensured. For a constant shock speed case, post-shock momentum is constant and so this treatment does not lead to error. However, for a strongly decelerating shock trajectory this can manifest as a non-physical drop in pressure toward the rear of the slug as slices at the rear travelling faster are not able to communicate their momentum for pressure with other slices toward the front. This is addressed indirectly in LASTA by imposing a constraint on the lagranges that pressure must not decrease moving upstream from the shock, which follows the observation in [26] that static pressure traces behind shocks increase monotonically until the contact discontinuity, even for strongly accelerating or decelerating trajectories. While this approach is adequate for many shock tube cases, it precludes the use of LASTA to model expansion tube experiments where test gas properties are strongly affected by expansion waves originating from the driver.

Table 1 Comparison of the capabilities of several widely used shock tube modelling tools

Code	A-priori / A-posteriori	Dimensionality	Non-Eq	Boundary Layer	Shock Trajectory	Computational Cost
ESTCj [9] / PITOT [11]	Both	0D	N	N	N	$
L1d [27]	Pre	1D	Y	~	N	$$$
NESS [28]	Both	Quasi-1D	Y	~	N	$
POSHAX [17]	Pre	Quasi-1D	Y	~	N	$$
Eilmer 4 [29] / US3D [16]	Pre	2D / 3D	Y	Y	N	$$$$$
FROSST [30]	Pre	2D	N	Y	N	$$
LASTA [24, 25]	Post	Quasi-1D	N	~	Y	$

In this paper improvements to LASTA are presented which include a rigorous treatment of the pressure relaxation process. The model utilises commonly available experimental data, namely shock trajectory and pressure traces, to extract additional information about the test slug. The governing equations and model methodology are presented, followed by preliminary results and validation against experimental data and previous versions of LASTA.

II. Methodology

The model, denoted LASTA 2.0, idealises the test slug as a one dimensional, inviscid core surrounded by a growing boundary layer, as shown in Figure 2. The model is conceived in the shock reference frame with x representing the distance behind the shock, $x \in [0, \ell]$, where 0 is the shock front and ℓ is the contact surface. The shock travels right to left at speed $-\Lambda$ in the inertial frame. The test gas travels at speed u in the inertial frame and $u + \Lambda = u'$ in the shock frame. The one dimensional Euler equations are solved at each time point t along the supplied experimental shock trajectory with a source term to represent mass removal by the boundary layer. The domain size or slug length, ℓ, is allowed to vary along the length of the shock trajectory based on the mass balance between the shock addition and boundary layer subtraction. The size of the test slug and hence the test time is determined by the location where the mass flow consumed by the boundary layer matches the mass flow processed by the shock. Two boundary conditions are imposed on the model:

1) The primitive variables (ρ, u, p) immediately behind the shock at each time point are set by the shock trajectory
2) The pressure profile at the final time point is set by the user, ideally experimental values obtained from a static pressure transducer

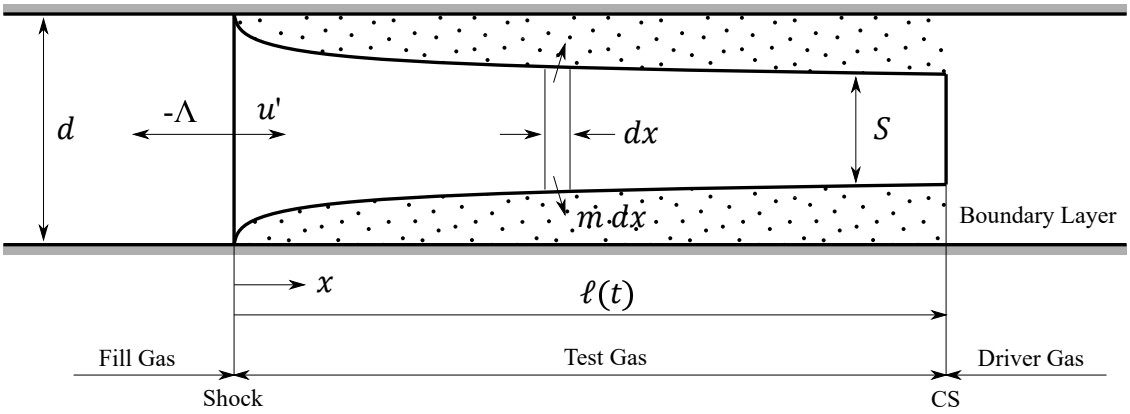

Fig. 2 Diagram of the model domain.

A. Core flow governing equations

The derivation of the model governing equations is presented in this section. Consider a thin slab of test gas of length dx as shown in Figure 3. Here, surface 1 (F_1) represents the left edge of the slice of test gas, surface 2 (F_2) represents the edge of the boundary layer, and surface 3 (F_3) represents the right edge of the slice of test gas. We wish to determine the fluxes of conserved quantities, mass, momentum, and energy, across the three surfaces so that we may establish the governing equations for the model.

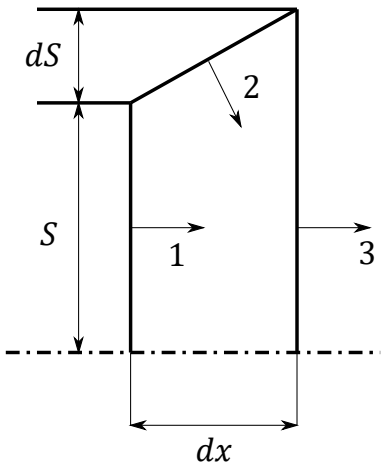

Fig. 3 An infinitesimally thin slice of test gas

The fluxes of mass, momentum, and enthalpy crossing the surfaces 1, 2, and 3 are given by:

$$F_1 = S\rho(u-\Lambda)\begin{bmatrix}1\\u\\h^0\end{bmatrix} + \begin{bmatrix}0\\Sp\\S\Lambda p\end{bmatrix} \tag{1}$$

$$F_2 = S\rho(u-\Lambda)\begin{bmatrix}1\\u\\h^0\end{bmatrix} + \begin{bmatrix}0\\Sp\\S\Lambda p\end{bmatrix} + d\left(S\rho(u-\Lambda)\begin{bmatrix}1\\u\\h^0\end{bmatrix} + \begin{bmatrix}0\\Sp\\S\Lambda p\end{bmatrix}\right) \tag{2}$$

$$F_3 = dS\rho(u-\Lambda)\begin{bmatrix}1\\u\\h^0\end{bmatrix} + dS\begin{bmatrix}0\\p\\\Lambda p\end{bmatrix} - dx\rho vl\begin{bmatrix}1\\u\\h^0\end{bmatrix} + \frac{\partial S}{\partial t}\rho\begin{bmatrix}1\\u\\e^0\end{bmatrix} \tag{3}$$

The time derivative of mass, momentum, and enthalpy in the inviscid core flow is given by:

$$\frac{\partial}{\partial t'}\begin{bmatrix}S\rho\\S\rho u\\S\rho e^0\end{bmatrix} = \frac{\partial}{\partial t'}\begin{bmatrix}\rho\\\rho u\\\rho e^0\end{bmatrix} = -\frac{\partial}{\partial x}\begin{bmatrix}\rho u'\\\rho u'u + p\\\rho u' h^0 + \Lambda p\end{bmatrix} - \rho\frac{vl}{S}\begin{bmatrix}1\\u\\h^0\end{bmatrix} \tag{4}$$

Where Λ is the shock speed, $u' = u - \Lambda$, u, e^0, and h^0 are velocity, total energy, and enthalpy in the inertial frame. v is a radial velocity. Equation 4 is the conservative form of the one dimensional Euler equations with a source term representing the boundary layer mass removal. Continuity of mass fluxes requires that the quantity vl/S is constant in the core flow and can be evaluated at a given radial position as:

$$\frac{vl}{S} = \frac{2\pi r v}{\pi r_1^2} = \frac{2v}{r} \tag{5}$$

Typically, r is set as the radius at the edge of the boundary layer. For large-diameter facilities, r is approximately the geometric radius of the tube. The term vl/S acts as a mass injection or removal mechanism and suppresses the need to

evaluate boundary layer displacement and velocity thicknesses to solve the model. A frame transformation, the details of which are included in Appendix A, is necessary to move the model to the shock frame. The resulting, Lagrangean, system of equations is shown in Equation 6.

$$\frac{\partial}{\partial t'}\begin{bmatrix}\rho\\u\\p\end{bmatrix} = -\begin{bmatrix}u' & \rho & 0\\0 & u' & \rho^{-1}\\0 & \rho a^2 & u'\end{bmatrix}\frac{\partial}{\partial x}\begin{bmatrix}\rho\\u\\p\end{bmatrix} - \rho\frac{2v}{r_1}\begin{bmatrix}1\\0\\a^2\end{bmatrix} \tag{6}$$

A final transformation is necessary to obtain the governing equations in characteristic form, which is achieved by solving the eigenvalue problem, yielding:

$$\frac{\partial}{\partial t'}\begin{bmatrix}w^{(1)}\\w^{(2)}\\w^{(3)}\end{bmatrix} = -\begin{bmatrix}u' & 0 & 0\\0 & u'+a & 0\\0 & 0 & u'-a\end{bmatrix}\frac{\partial}{\partial x}\begin{bmatrix}w^{(1)}\\w^{(2)}\\w^{(3)}\end{bmatrix} - a\frac{2v}{r_1}\begin{bmatrix}0\\1\\-1\end{bmatrix} \tag{7}$$

This system of equations governs the inviscid core in the present work. The flow equations, closed by the thermochemistry model equations, are discretised using a first order accurate finite difference method and cast as a large system of coupled algebraic equations. The system is solved using Newton iterations based on in-exact Jacobian matrices, the approach to solution of the algebraic system is presented in further detail in Appendix B.

B. Boundary layer governing equations

Presently, the boundary layer is not explicitly modelled, but its effects on the core flow are included by assuming the radial velocity v behaves according a local similarity approximation proposed by Mirels [1]. Using this approximation, the radial velocity at the edge of the boundary layer can be evaluated as:

$$v = \frac{\rho_{e,0}u_{e,0}\sqrt{\ell_m}}{\rho\sqrt{\ell}} \tag{8}$$

where ℓ is the distance from the shock, $\rho_{e,0}$, $u_{e,0}$ are the immediate post-shock density and velocity in the shock reference frame, ρ is the density in the test slug evaluated at ℓ, and ℓ_m is the maximum slug length. The maximum slug length is given by Mirels as:

$$\ell_m = \frac{d^2}{16\beta^2}\left(\frac{\rho_{e,0}}{\rho_{w,0}}\right)^2\frac{u_{e,0}}{\Lambda - u_{e,0}}\frac{u_{e,0}}{\upsilon_{w,0}} \tag{9}$$

where d is the tube diameter, β is a calculated shape factor, $\rho_{w,0}$ and $\upsilon_{w,0}$ are the density and kinematic viscosity evaluated at the tube wall temperature, and Λ is the shock speed as before. Mirels' analysis provides estimates of the shape factor β behind a shockwave:

$$\beta = C_M^{\alpha}1.59\left(1 + \frac{1.796 + 0.802W}{WZ - 1}\right) \tag{10}$$

where

$$C_M = \frac{\rho_{sh}\mu_{sh}}{\rho_{w,sh}\mu_w} \tag{11}$$

Here, $W = u_w/u_{sh}$ and $Z = \frac{\gamma+1}{\gamma-1}$. C_M corrects for boundary layer shape to account for changes in the freestream properties where α is an empirical constant, 0.48 here. These equations are evaluated to obtain the radial velocity profile along the test slug which can then be used to evaluate the source term. It should be noted that Mirels' analysis was developed for a steady, constant shock speed case, whereas here it is applied for a non-uniform, unsteady shock speed, the physical implication being that it is assumed that the entire boundary layer shape is instantly resized for changing shock speed. Previous work has shown that this assumption is sufficient for many typical shock tube cases [24].

C. Treatment of experimental inputs

The model relies on two experimental inputs as boundary conditions. The first is a shock speed trajectory in the form of $x - t$ data where x is a vector of timing station locations and t is the arrival time of the shock at each location. For the cases presented in this work, maximum and minimum arrival time is selected manually for each timing station and assigned an uncertainty based on the selection width. The shock speed is simply calculated as $u_s = \Delta x/\Delta t$ so if n stations are available a vector of $n - 1$ shock speeds is produced. In order to discretise the shock trajectory a high order polynomial is fitted to the shock speed vector and average arrival time i.e. a time between two station arrival times equidistant from each. The polynomial is evaluated at each simulation time point and the resulting shock speed is used to determine the flow properties via a normal shock relation.

The second experimental input is the pressure distribution in the test slug, obtained via a wall pressure trace or Pitot probe. Pressure sensors in impulse facilities can exhibit a number of non-ideal behaviours which should be considered when integrating them into the simulation. Firstly, they can be relatively noisy and thus a degree of smoothing or fitting is necessary. Secondly, they have a limited bandwidth and response time, in the case of PCB113s approximately 500 kHz and 2 µs respectively, so flow features with timescales less than these are not resolved. This manifests as an inherent uncertainty in the time of shock arrival. Thirdly, they respond to thermal shock which can limit the range of usable data. In the present work a moving average fit is applied to the pressure traces beginning at the time determined to coincide with shock arrival. The width of the averaging window is varied depending on the signal to noise ratio of the trace but is typically 5 corresponding to 2 µs. The program accepts the pressure distribution as a space wise distribution through the test slug and thus the experimental data must be converted from a dependence on time to a dependence on space. This is done simply by multiplying the time values by the shock speed at the timing station.

D. Method of solution

The characteristics $w^{(2)}$ and $w^{(3)}$ may be thought of as sound waves travelling through the test slug, $w^{(2)}$ originating from the shock front and $w^{(3)}$ originating from the driver gas. Figure 4a illustrates the directions of propagation for the $w^{(2)}$ and $w^{(3)}$ waves in a shock tube experiment where time progresses from top to bottom. Accurate numerical modelling of the effect of the $w^{(3)}$ characteristic on the test slug properties with forward time integration would require a tight constraint on the position of the contact surface as a boundary condition. Unfortunately, experimental information about the position of the contact surface is difficult to obtain non-intrusively and is typically unavailable, thus, the effect of $w^{(3)}$ on the test slug cannot be calculated via forward time integration. However, $w^{(3)}$ waves will ultimately propagate through the test slug to the shock front, so $w^{(3)}$ is known indirectly through its effect on the future trajectory. By integrating $w^{(3)}$ backwards in time, the approach taken here and shown in Figure 4b, the test gas is within the domain of influence of the shock with respect to $w^{(3)}$ and the full test slug history may be calculated using the shock trajectory and final pressure profile as boundary conditions.

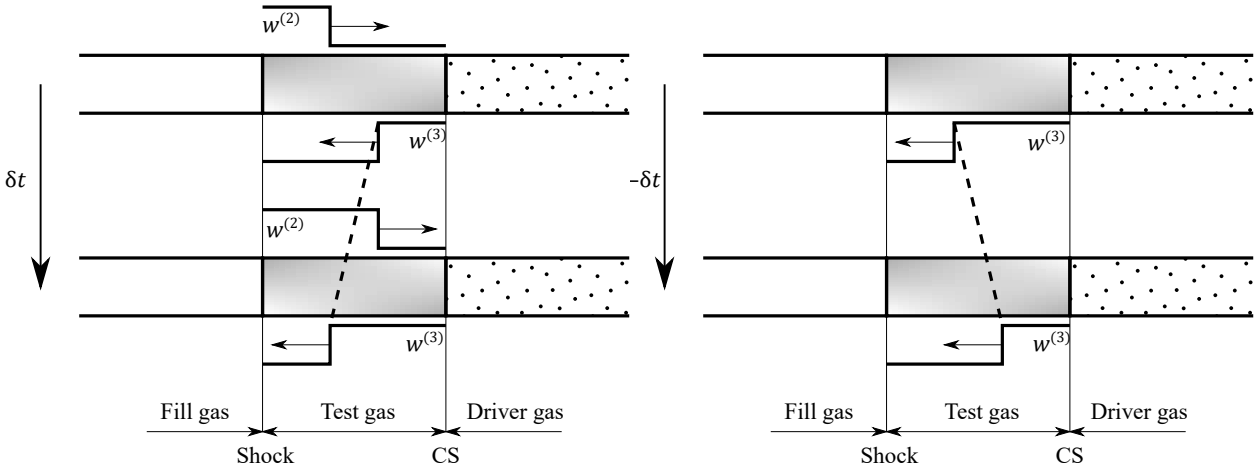

(a) Forward integration **(b) Backward integration**

Fig. 4 Time integration for the $w^{(3)}$ characteristic

The $w^{(3)}$ characteristic waves travel at a finite speed and thus their inclusion via the pressure boundary condition

will influence only a subset of the solution domain. This is illustrated by Figure 5, an x-t diagram of a shock tube experiment in the shock reference frame. Figure 5a shows the wave processes modelled by LASTA 1.0, and Figure 5b shows the additional wave processes modelled by LASTA 2.0 as a result of the new boundary condition. It can be seen that the influence of the $u + a$ waves on the slug properties becomes more significant toward the rear of the slug as more waves have had time to pass through this region. Necessarily, the influence of $u - a$ waves, although still significant, becomes less important toward the rear of the slug. LASTA 1.0 assumes that the relative flow within the test slug is low subsonic and that the time it takes for sound waves to propagate along the slug length is negligible compared to the duration of the trajectory, or more precisely that within a typical acoustic propagation time variations in shock speed are negligible. This assumption is addressed by LASTA 2.0 and improvement is expected in the region where the $u + a$ waves may propagate.

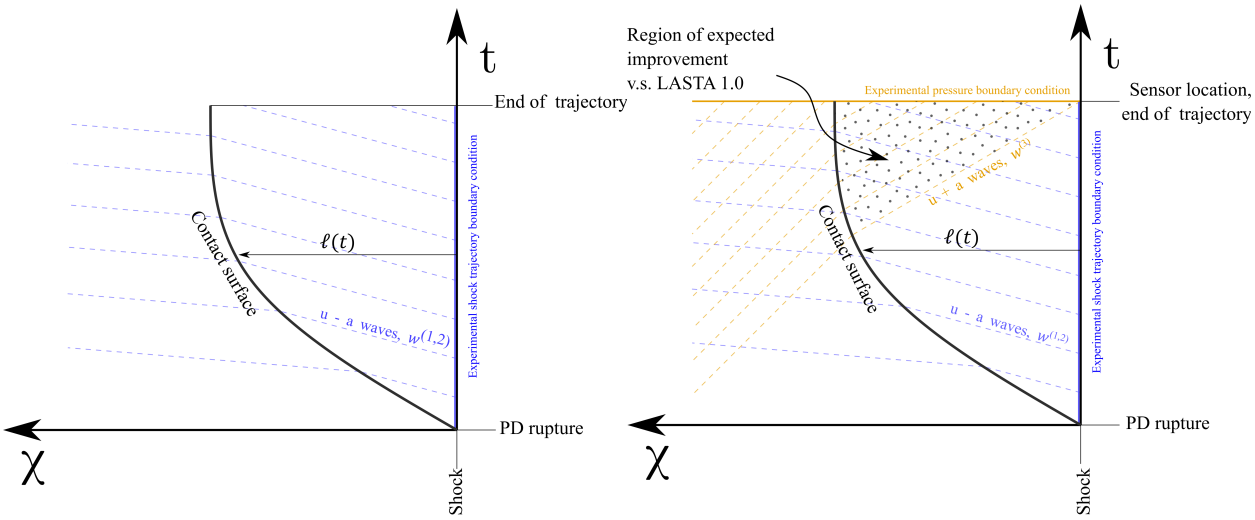

(a) LASTA 1.0 **(b) LASTA 2.0**

Fig. 5 Diagrams of the wave processes modelled explicitly in each version of LASTA. The diagrams are representative of the processes occurring in a real experiment, but are not drawn to scale

It should be noted that, although pressure measurements are used as a boundary condition here, it is possible in principle to use other experimental data, such as temperature inferred from heat transfer gauge measurements, as a boundary condition. It is also possible to move the boundary condition upstream or downstream, assuming experimental data is available, to the location of greatest interest.

The system of governing equations is solved using a finite different method. The forward characteristics are evaluated at the ith spatial point and kth time point as:

$$\delta^t w^{(1)}_{i,k} + \frac{\Delta t}{\Delta x} u'_{i,k} \delta^+ w^{(1)}_{i,k} = 0 \tag{12}$$

$$\delta^t w^{(2)}_{i,k} + \frac{\Delta t}{\Delta x} \left(u'_{i,k} + a_{i,k} \right) \delta^+ w^{(2)}_{i,k} + 2 \frac{a_{i,k} v_{i,k}}{r} = 0 \tag{13}$$

where

$$\delta^t w^{(1)}_{i,k} = \rho_{i,k} - \rho_{i,k-1} - \frac{1}{a^2_{i,k}} \left(\rho_{i,k} - \rho_{i,k-1} \right) \tag{14}$$

$$\delta^+ w^{(1)}_{i,k} = \rho_{i,k} - \rho_{i-1,k} - \frac{1}{a^2_{i,k}} \left(\rho_{i,k} - \rho_{i-1,k} \right) \tag{15}$$

$$\delta^t w^{(2)}_{i,k} = u_{i,k} - u_{i,k-1} + \frac{1}{\rho_{i,k} a_{i,k}} \left(p_{i,k} - p_{i,k-1} \right) \tag{16}$$

$$\delta^+ w^{(2)}_{i,k} = u_{i,k} - u_{i-1,k} + \frac{1}{\rho_{i,k} a_{i,k}} \left(p_{i,k} - p_{i-1,k} \right) \tag{17}$$

The backward characteristic is evaluated as:

$$\delta^t w^{(3)}_{i,k+1} + \frac{\Delta t}{\Delta x}\left(u'_{i,k} - a_{i,k}\right)\delta^+ w^{(3)}_{i,k} + \frac{2a_{i,k}v_{i,k}}{r} = 0 \tag{18}$$

where

$$\delta^t w^{(3)}_{i,k+1} = u_{i,k+1} - u_{i,k} - \frac{1}{\rho_{i,k}a_{i,k}}\left(p_{i,k+1} - p_{i,k}\right) \tag{19}$$

$$\delta^+ w^{(3)}_{i,k} = u_{i,k} - u_{i-1,k} - \frac{1}{\rho_{i,k}a_{i,k}}\left(p_{i-1,k} - p_{i,k}\right) \tag{20}$$

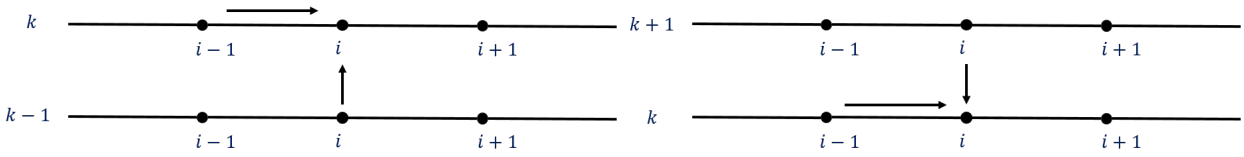

(a) entropy and right running sound wave **(b) left running sound wave**

Fig. 6 Finite difference scheme

The grid spacing Δx in equations 12,13 and 18 is constructed as

$$\Delta x = \ell \Delta \eta \tag{21}$$

where η is a non-dimensional coordinate with value 0 at the shock surface and 1 at the contact discontinuity. In order for the model to be solvable, an additional relation is needed to determine the slug length ℓ. The additional equation is obtained by imposing that at the contact discontinuity the relative velocity in the shock frame of reference matches the rate of change of the test slug length:

$$u' = \frac{d\ell}{dt} \tag{22}$$

III. Validation

LASTA 2.0 was validated against a series of numerical simulations by Satchell et al. [26], as was done for LASTA 1.0 [24]. These validation cases use an ideal gas model and thus remove the complication of thermochemistry. The results from application of LASTA 2.0 to more complex experimental trajectories are presented in Section IV.

A. FROSST

The FRamework for Overset Simulation of Shock Tubes (FROSST) is an axisymmetric, explicit, structured finite volume code for solution of the Navier-Stokes equations for ideal gas simulation of shock tube flows. The code is written using an overset formulation that allows a highly refined grid to be attached to both shock and contact discontinuity with the intention of reducing computational cost when compared to typical axisymmetric shock tube solvers. FROSST has the capability to model the effect of primary diaphragm opening, allowing for the production of non-uniform shock trajectories. FROSST has been validated against a number of historical and canonical shock tube cases and serves as the benchmark for comparison to LASTA 2.0 in the present work. FROSST is described in greater detail by Satchell et al. [30].

B. Test cases

Satchell et al. [26] devised three shock tube test cases using the FROSST code with the same final shock speed but differing initial shock speeds, thus allowing the effect of non-uniform shock speed to be evaluated. The trajectories are shown in Figure 7, consisting of a strongly decelerating, strongly accelerating, and relatively constant shock speed case. All cases result in a shock speed of 2100 m s^{-1} at a distance 8 m from the primary diaphragm. Pure Argon was used as the test gas at an initial pressure and temperature of 66.7 Pa and 300 K respectively. A tube diameter of 100 mm was selected.

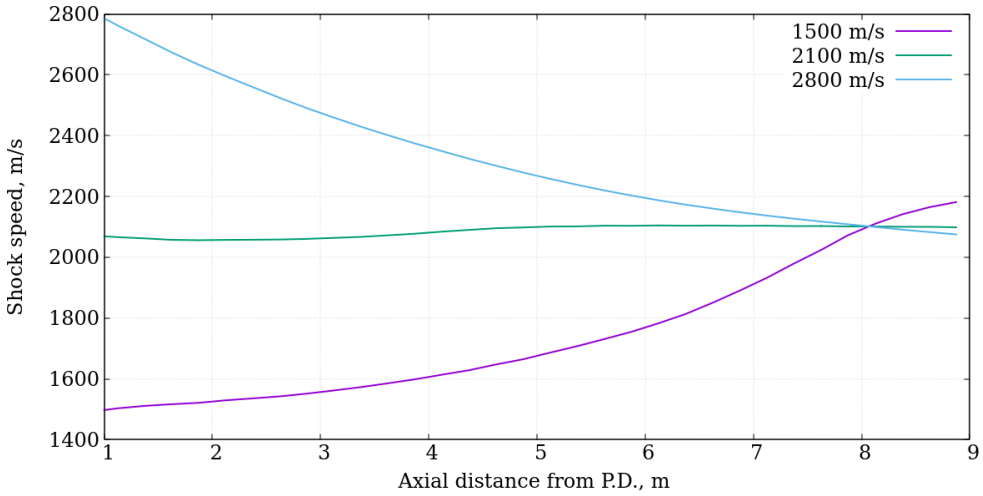

Fig. 7 Shock speed as a function of distance from the primary diaphragm for the three test cases

For all data presented herein the LASTA 2.0 domain was discretized into 72 points behind the shock with 5 % grid clustering toward the shock front, that is, $x(i) = x(i-1) + dx(i)$ where $dx(i) = 1.05dx(i-1)$ with $dx(1) = 0.005$ m. The supplied shock trajectory was discretized into 128 time points. Simulations were run on a workstation with an Intel(R) Xeon(R) W-2265 CPU clocked at 3.50 GHz and 64.0 GB of RAM. The average run time for the trajectories was 26.5 s.

For each simulation, the full shock trajectory, and the pressure profile at 9 m from the primary diaphragm from the FROSST test cases were used as boundary conditions. The pressure profile at any location along the length of the tube may in principle be used as the boundary condition. 9 m was selected so that the profiles at 8 m, the location where the test case shock trajectories converge on 2100 m s^{-1}, were within the domain of influence of but not explicitly set by the new boundary condition. This arrangement is analogous to interrogating a location slightly upstream of a pressure transducer in an experimental facility, which is ultimately the intended use case.

C. Results

LASTA 2.0 pressure and temperature profiles at various points along the shock trajectory are compared to results from LASTA 1.0 and FROSST for the same cases. Here, as discussed in Section II.D, LASTA 2.0 is expected to improve over LASTA 1.0 in the region where sound waves emanating from the driver that are encapsulated in the pressure boundary condition overlap with the test slug. This region increases in size as the boundary condition is approached in time, beginning with improvements at the rear of the slug and ending at the boundary condition its self where the entire slug is affected. Figures 8 and 9. show pressure and temperature profiles at 8 m, 8.5 m, and 9 m from the primary diaphragm. Each of these locations are within the domain of influence of the boundary condition and thus improved agreements for pressure between FROSST and LASTA 2.0 versus LASTA 1.0 are expected for all, particularly toward the rear of the test slug.

LASTA 2.0 pressure profiles exactly match those of FROSST at 9 m from the diaphragm, the location of the boundary condition. LASTA 2.0 pressure profiles at 8 m and 8.5 m also show excellent agreement with FROSST where the difference is less than 1 % for all cases. LASTA 1.0 results for the 1500 m s^{-1} case differ from the other two approaches, albeit by a maximum of 3.5 %, at each location. This has previously been attributed to 2D-effects, namely the arrival of a jet of driver gas and subsequent deformation of the contact discontinuity in the FROSST simulations, which are not accounted for in the 1D LASTA 1.0 simulation. Although LASTA 2.0 is also a 1D code, these pressure deviations are not apparent, a fact that can only be attributed to the inclusion of the new boundary condition.

Profiles of temperature, which are not set explicitly as a boundary condition in LASTA 2.0, agree with LASTA 1.0 and FROSST within 1% except in the decelerating case where divergence begins at 150 µs. This is due to the arrival of a cold jet of driver gas in the FROSST simulation which is not accounted for in LASTA 2.0. The fact that LASTA 1.0 does not also diverge with LASTA 2.0 is an illustration of the LASTA 1.0 'pressure limiter' in effect. Rather than solving for the full Euler equations for one dimensional flow including conservation of momentum, LASTA 1.0 features a constraint on pressure that mimics the effect of momentum exchange between gas slices. This follows the

observation that, even for strongly decelerating cases, pressure behind the shock tends to increase monotonically until the contact discontinuity. This manifests in LASTA 1.0 as a condition that pressure must not decrease moving upstream from the shock. This is a non-physical constraint that improves agreement between LASTA 1.0 and many shock tube test cases, but precludes application of LASTA 1.0 to test cases where upstream waves are dominant, most notably the expansion tube. Closer agreement between LASTA 2.0 and FROSST could be achieved by adopting the LASTA 1.0 pressure limiter, however retaining the rigorous treatment of the test slug in LASTA 2.0 allows for the addition of non-equilibrium thermochemistry which is not possible in LASTA 1.0

The test times predicted by LASTA 2.0 show improved agreement with FROSST compared with LASTA 1.0. Since pressure across the contact discontinuity must be equal, the FROSST temperature profiles in Figure 9 provide the best indication of the extent of the test slug, the sharp drop in each case corresponding to driver gas arrival. Satchell et al. [24] highlighted that the cause of the LASTA 1.0 test time over prediction was two fold:

1) The one dimensional nature of the code could not account for a multidimensional effect in the accelerating case, namely the jetting of driver gas into the rear 35% of the test slug leading to a decrease in test time
2) Inability to account for additional loss of test slug mass past the contact discontinuity

These effects are still present, but their effect is reduced in LASTA 2.0 as additional information about the contact surface state is included in the pressure boundary condition, which is in turn included in the test slug state via backwards time integration. The greatest difference is evident in the strongly accelerating case, where the LASTA 1.0 predicted test time is 15% larger than that of LASTA 2.0. This is expected, as in this case the cause of the shock acceleration is the contribution of pressure waves from the driver and thus their exclusion leads to error.

LASTA 2.0 test time predictions still differ from FROSST, in some cases under predicting and some cases over predicting. This is expected, since LASTA 2.0 cannot fully account for the multidimensional nature of the contact discontinuity as a 1D code. The difference is in part due to boundary layer implementation. The Mirels model was developed under the assumption of a steady, constant shock speed, which is not the case here. Mirels' model is re-evaluated at each time point in the simulation, the physical implication being that the boundary layer instantly resizes to match the current shock speed. This is not the case in reality as the boundary layer would require time to resize and would therefore entrain a different amount of mass from the test slug, leading to a different test time. Implementation of an unsteady boundary layer solution would likely improve agreement with FROSST.

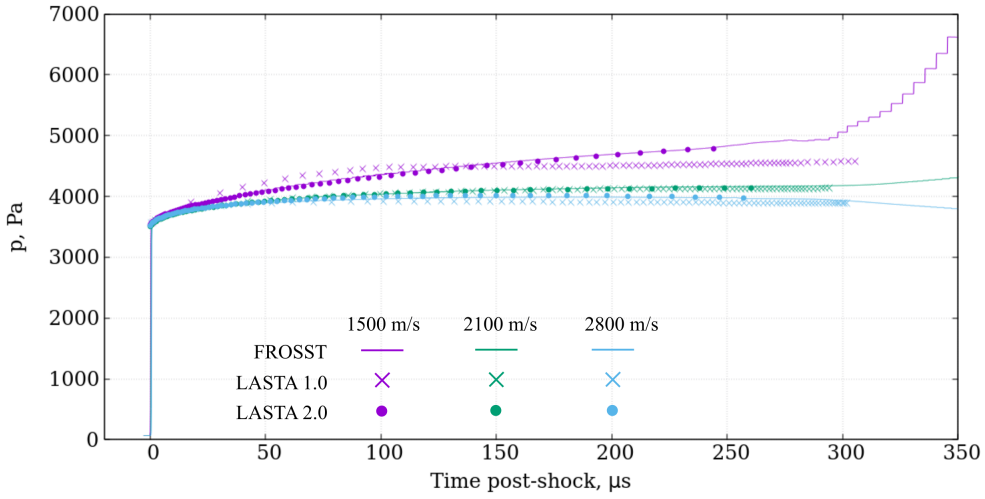

(a) 8 m

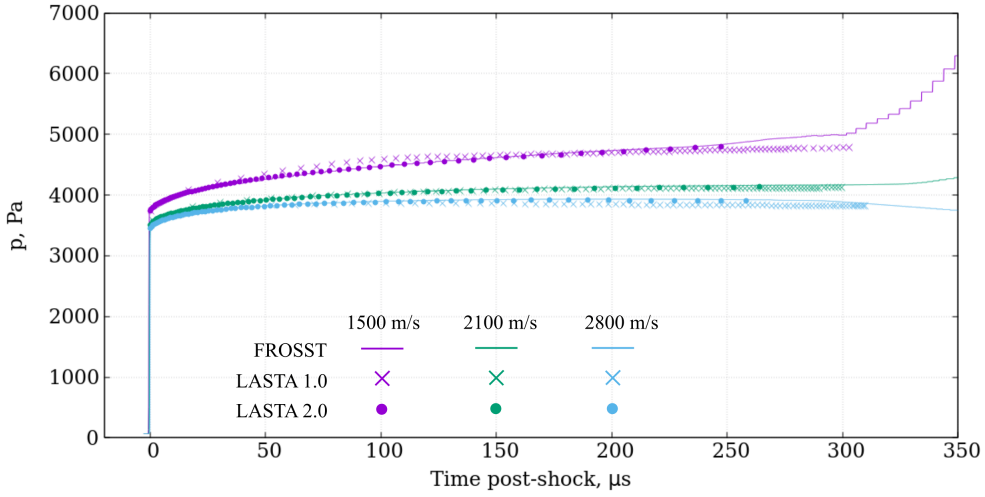

(b) 8.5 m

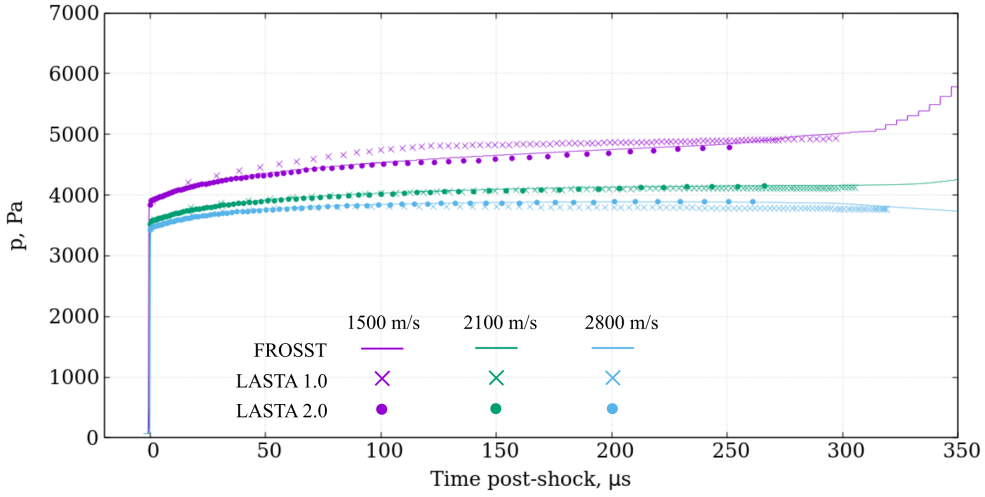

(c) 9 m (**LASTA 2.0 boundary condition location**)

Fig. 8 Profiles of pressure obtained a three axial locations along the shock tube from FROSST, LASTA 1.0, and LASTA 2.0

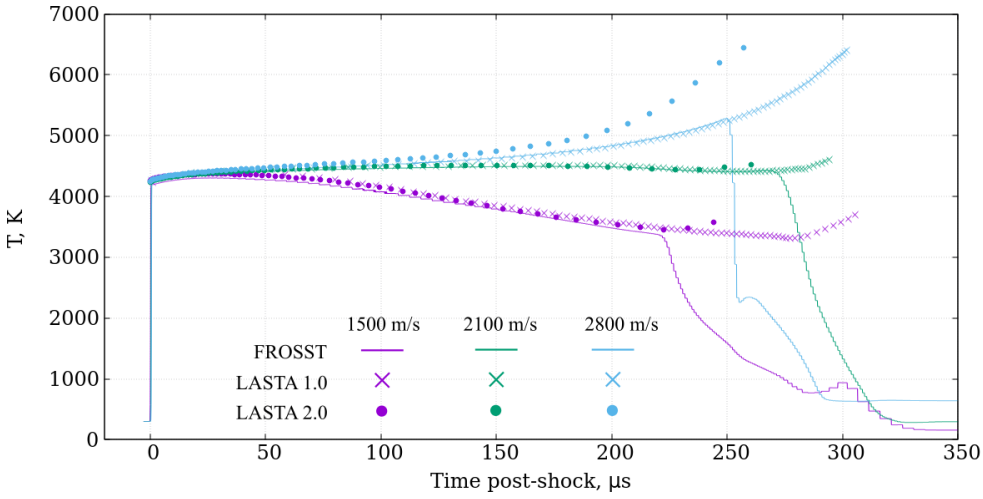

(a) 8 m

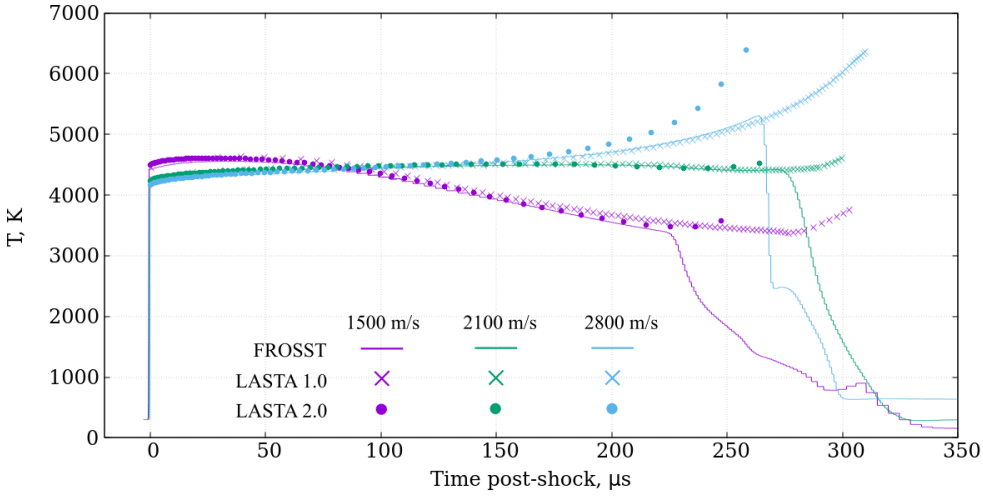

(b) 8.5 m

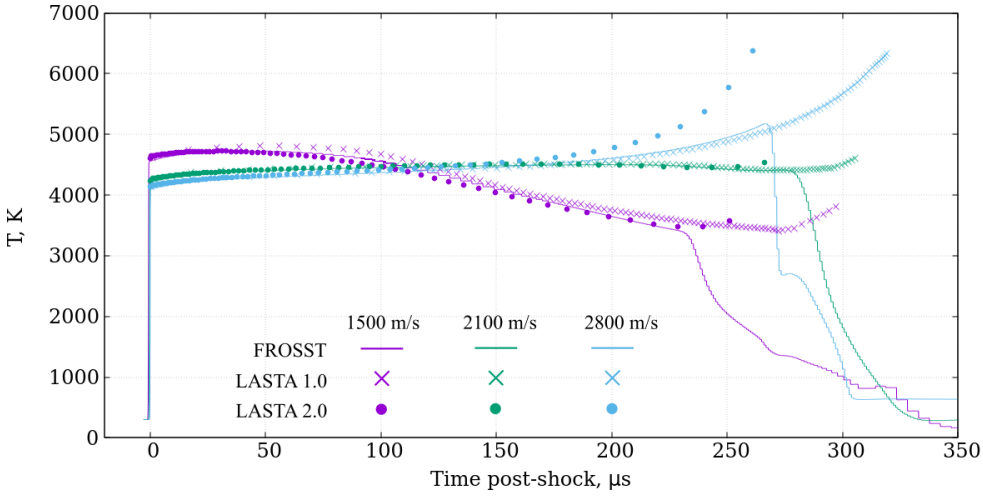

(c) 9 m (**LASTA 2.0 boundary condition location**)

Fig. 9 Profiles of temperature obtained a three axial locations along the shock tube from FROSST, LASTA 1.0, and LASTA 2.0

IV. Application

The LASTA 2.0 is now applied to experimental cases where more complex upstream waves are present. All experiments were performed in the T6 Stalker Tunnel and have previously been used as validation for LASTA 1.0 [25].

A. Oxford T6 Stalker Tunnel

T6 is a multi-mode hypersonic wind tunnel, a complete overview of T6 can be found in Collen [3]. The free-piston driver, which generates pressures on the order of 50 MPa during a shot, may be coupled to a range of downstream components to allow operation of the facility as either a shock tube (ST), expansion tube or expansion tunnel (ExT), or reflected shock tunnel (RST). T6 offers the only expansion tube capability in Europe with test times between 20 and 150 µs.

During an experiment, a piston weighing either 36 or 90 kg is accelerated to speeds of approximately 300 m s^{-1} by high pressure air known as the reservoir gas. The gas in the volume between the piston head and the primary diaphragm, typically low pressure helium, is polytropically compressed to the diaphragm rupture condition by the piston motion. In the present work 3 x 0.3 mm score depth stainless steel diaphragms are used with a rupture pressure of 10.0 MPa and temperature of 4000 K. This high pressure, high temperature driver gas unsteadily expands into the 'Shock Tube', shown in Figure 1, forming the shock wave that is studied at the end of the facility. Static pressure in the driven tubes is measured by between 9 and 17 PCB113 piezoelectric pressure transducers depending on the mode of operation. Shock speed is inferred by measuring the difference in arrival time between the transducers.

The experiments included here were performed in the T6 Aluminium Shock Tube (AST), shown schematically in Figure 10. This configuration features a conical expansion nozzle at 3.8 m from the primary diaphragm which increases the facility internal diameter from 96.3 mm to 225 mm. A larger internal diameter offers many advantages if emission spectroscopy is utilised, which is not the case here. Further details about the AST are provided by [3].

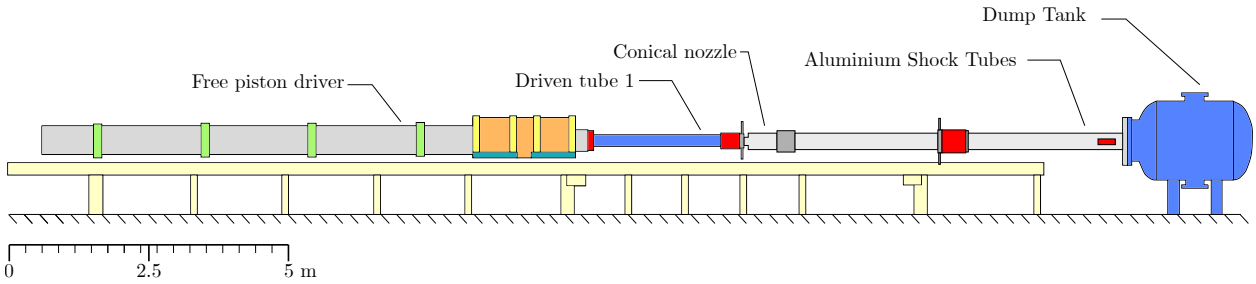

Fig. 10 Schematic diagram of the T6 Stalker Tunnel in aluminium shock tube mode (AST)

B. Test cases

Two test cases, detailed in Table 2, are considered. Both employed pure Argon as the test gas in an effort to minimise thermochemical effects. Equilibrium simulations of the post shock states indicate that only 0.1% of the test gas was ionized at any point. The experimental shock trajectories for the two cases are shown in Figure 11. Both cases feature deceleration after the conical expansion located at 3.8 m. Here, the pressure profile obtained from shock timing station 17 located at a distance 9.584 m from the primary diaphragm, is always used as the pressure boundary condition for LASTA 2.0 simulations. Both LASTA 1.0 and 2.0 simulations were begun at the 4.31 m from the primary diaphragm so as to exclude the conical expansion section. Grid discretisation and workstation settings remained the same as those specified in Section III.

Table 2 Initial pressures and shock speeds at the observation window for the experimental cases

Shot number	Fill pressure, Pa	Final shock speed, m/s
T6s212	133.2	2670
T6s214	66.6	3080

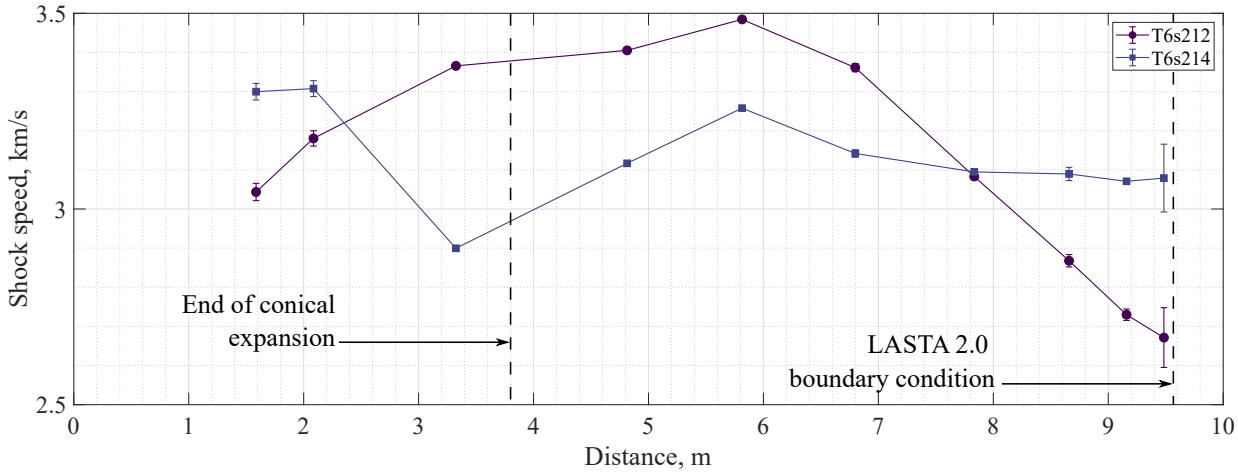

Fig. 11 Shock speed as a function of distance from the primary diaphragm for the two experimental test cases

C. Results

Pressure profiles obtained from experiment, LASTA 1.0, and LASTA 2.0 simulations for T6s212 are shown in Figure 12. Results are presented at locations corresponding to the three most downstream static pressure transducers available. STS-17, STS-15, and STS-13 are the names of the pressure transducers are they are located at axial distances of 9.584 m, 9.384 m, and 8.934 m from the primary diaphragm respectively. A 200 kHz bandpass filter has been applied to all experimental data presented. This case features strong shock deceleration between 6.0 and 9.5 m which is expected to highlight the differences between LASTA 1.0 and 2.0. LASTA 1.0 generally under predicts the experimental pressure profiles at all locations. Because conservation of momentum is not strictly enforced in LASTA 1.0, gas 'slices' at the rear of the slug that have a higher post shock speed are not able to exchange their momentum for pressure with slices further ahead. This manifests as a non-physical drop in pressure toward the rear of the slug. The effect is more apparent in the experimental data than the FROSST cases in Section III as shock deceleration occurs over a much shorter distance, 3.8 m versus 7.0 m.

LASTA 2.0 generally shows improved agreement with the experimental data. The domain of influence of the pressure boundary condition is evident in Figures 12a and 12b as the point where LASTA 2.0 profiles depart from LASTA 1.0. This point moves further back in the slug for timing stations further upstream. This is a demonstration of the utility of reverse time integration approach for shock tubes cases with strong shock speed non-uniformity as improved information is available not only at the location of the boundary condition, but also upstream of it.

Pressure profiles obtained from experiment, LASTA 1.0, and LASTA 2.0 simulations for T6s214 are shown in Figure 13. Better agreement between LASTA 1.0 and experiment is seen here because of the less extreme shock trajectory for this case. The shock speed profile is relatively flat and is therefore not expected to be a strenuous test case for the LASTA 1.0 methodology. The domain of influence of the new pressure boundary condition is again evident for this test case with LASTA 2.0 showing generally improved agreement with experimental data versus LASTA 1.0 in these regions.

Slug length predictions differ between each version of LASTA in both test cases. Although the theory of Mirels assumes a steady shock speed, it can be used here to provide upper and lower bounds for the expected slug lengths in each test case. Figure 14 and Table 3 summarise the predictions of Mirels' theory over the range of shock speeds in each experimental case expected at STS-17, 9.584 m from the primary diaphragm. It should be noted that Mirels' predictions are made assuming the trajectory began at the end of conical expansion, which will lead to an under-prediction of the experimental case where the test slug will have time to grow before and during the conical expansion. Both versions of LASTA tend to over-predict the test time compared the theory of Mirels. Notably, the LASTA 1.0 slug length predictions are much greater than those of LASTA 2.0 for the strongly decelerating T6s212 case. The reasons for the differing predictions are similar to those discussed in Section III, primarily that the one-dimensional nature of the codes cannot account for complex, multidimensional driver/test gas interactions.

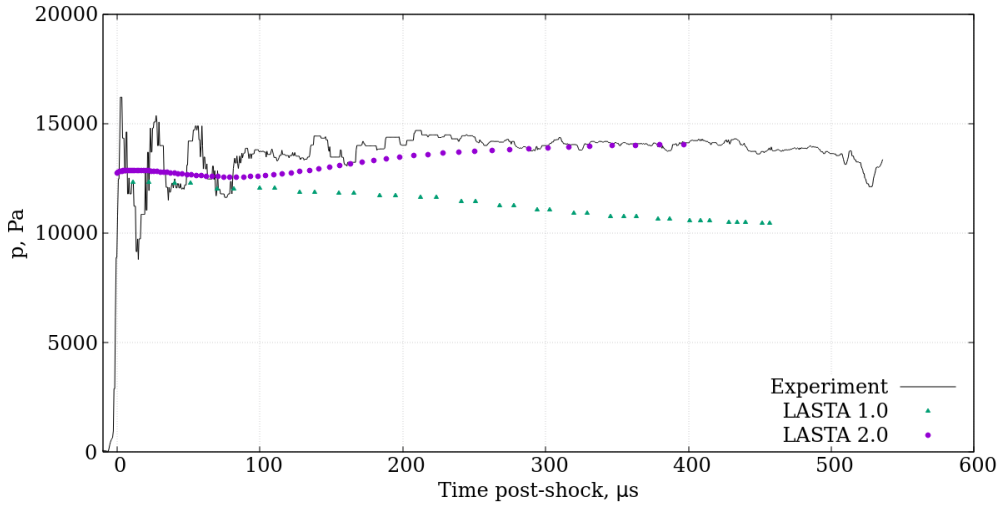

(a) STS-13, 4.62 m from simulation start, 8.934 m from P.D.

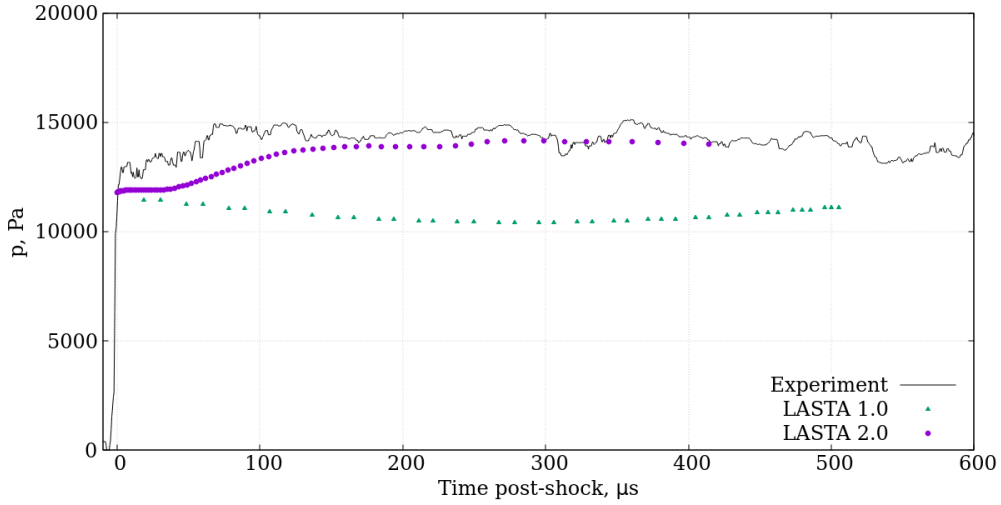

(b) STS-15, 5.07 m from simulation start, 9.384 m from P.D.

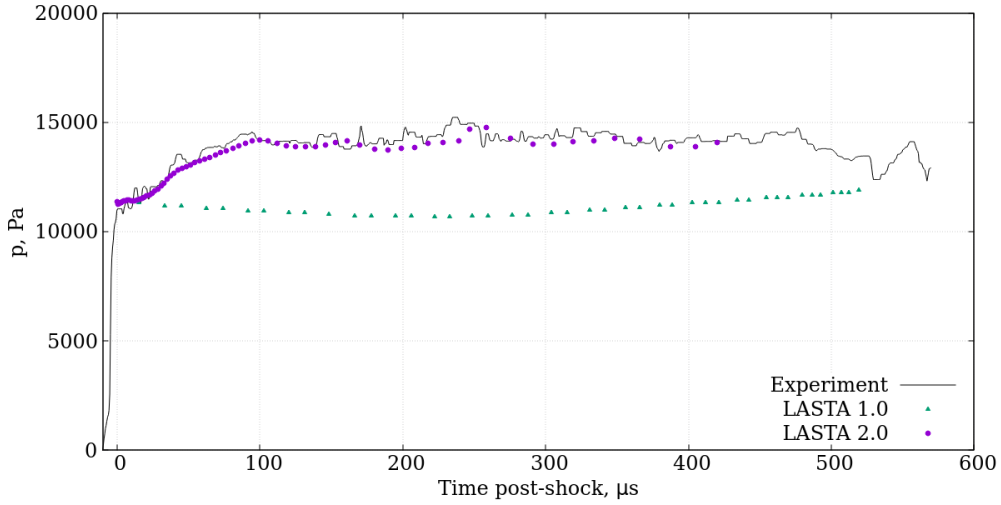

(c) STS-17, 5.27 m from simulation start, 9.584 m from P.D., LASTA 2.0 boundary condition

Fig. 12 Comparisons between experimental pressure profiles and those obtained from LASTA 1.0 and LASTA 2.0 for T6s212

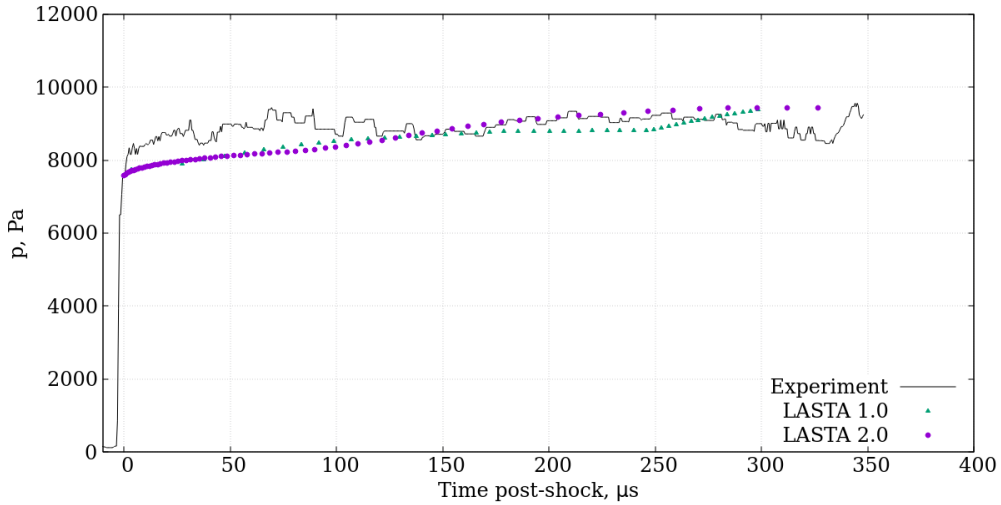

(a) STS-13, 4.62 m from simulation start, 8.934 m from P.D.

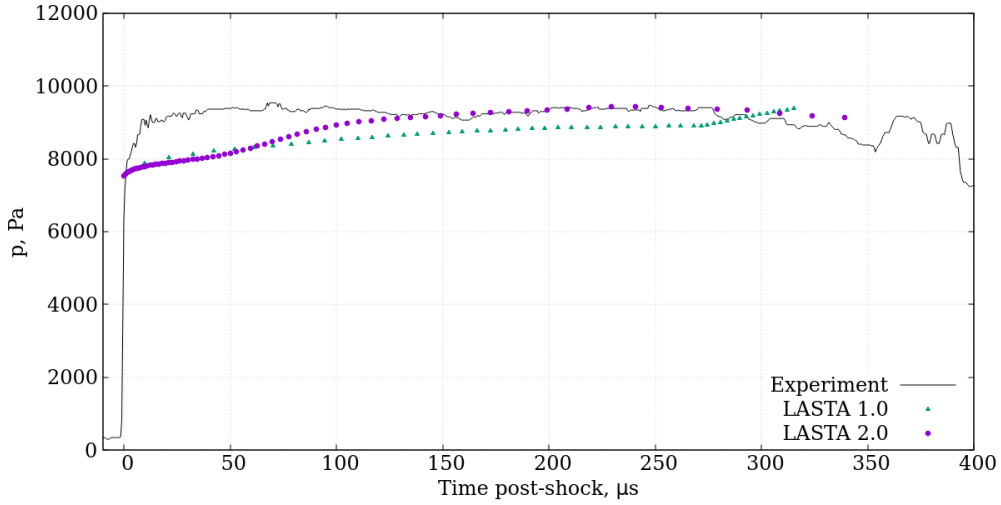

(b) STS-15, 5.07 m from simulation start, 9.384 m from P.D.

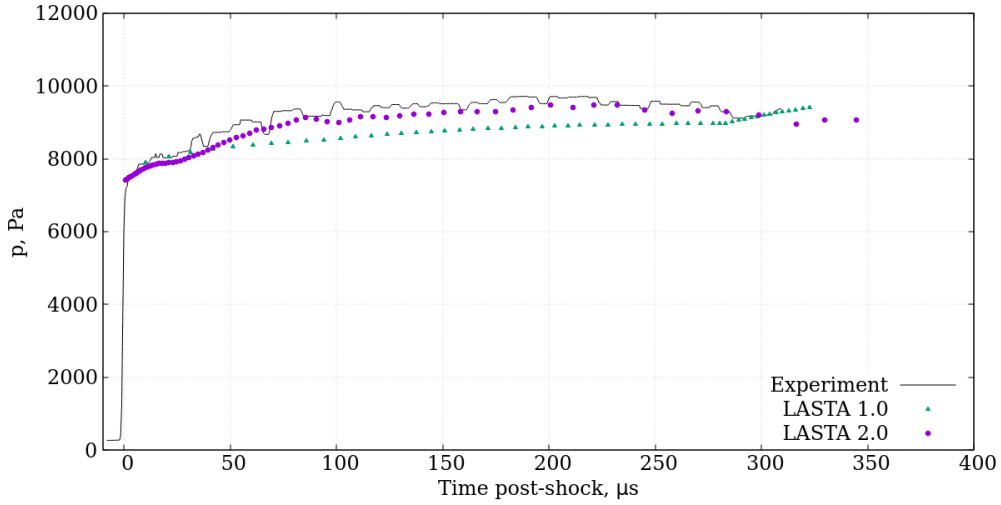

(c) STS-17, 5.27 m from simulation start, 9.584 m from P.D., LASTA 2.0 boundary condition

Fig. 13 Profiles of temperature obtained a three axial locations along the shock tube from FROSST, LASTA 1.0, and LASTA 2.0 for T6s214

Table 3 Summary of test time predictions at the location of STS-17

Shot Number	Fill pressure, Pa	Shock Speed Bounds, m/s	Steady Mirels Slug Length, m	Steady Mirels Slug Time, us	LASTA 1.0 Slug Time, us	LASTA 2.0 Slug Time, us
T6s212	133.2	2700 - 3500	0.826 - 0.875	236 - 324	520	424
T6s214	66.6	3000 - 3200	0.973 - 0.983	304 - 327	324	345

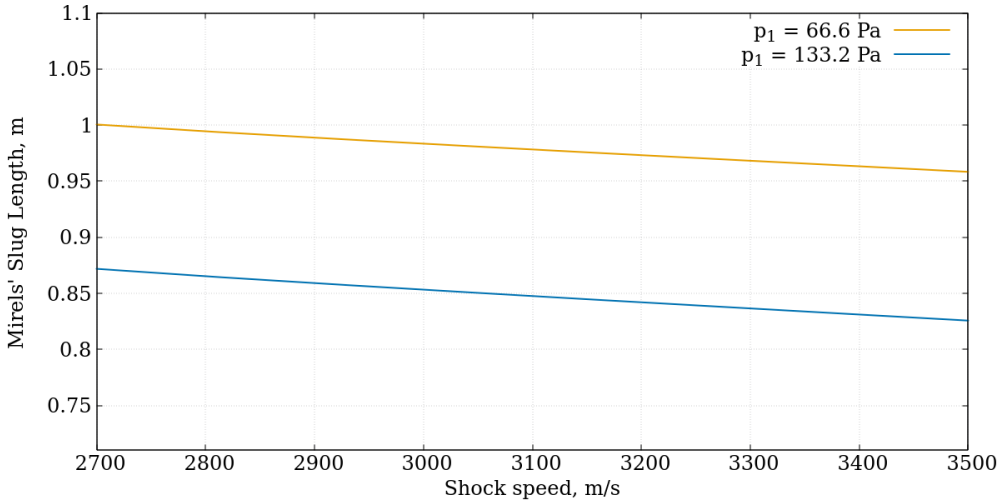

Fig. 14 Predictions of slug length at the location of STS-17 using Mirels' theory assuming a steady shock speed

V. Conclusion

A novel, rigorous approach to shock tube modelling has been validated against an established numerical tool and applied to several basic shock tube cases. It has been demonstrated that, via a reverse time integration method, it is possible to extract valuable information about wave trains originating from the driver gas by utilizing available pressure data as a boundary condition. This method removes the need for non-physical constraints on pressure that are present in previous attempts which allows for the implementation of non-equilibrium thermochemistry and ultimately application to expansion tube flow reconstruction. Improved agreement with experimental data has been demonstrated versus the previous version of the code in the region where corrections from the new boundary condition may propagate.

Acknowledgements

The authors would like to thank Dr. Matthew Satchell for his efforts in producing an extended dataset for the FROSST validation cases and for contributions to discussions about the work. The authors would also like to acknowledge Dr. Peter Collen and Alex Glenn who produced the T6 datasets used as test cases herein. J. Steer would like to acknowledge the European Space Agency for enabling this work by funding his studentship through the OSIP program.

A. Frame transformation

Define

$$dx = dy - \Lambda dt \tag{23}$$
$$d\phi = \frac{\partial \phi}{\partial x} dx + \frac{\partial \phi}{\partial t} dt \tag{24}$$
$$d\phi = \frac{\partial \phi}{\partial x} (dy - \Lambda dt) + \frac{\partial \phi}{\partial t} dt \tag{25}$$
$$d\phi = \frac{\partial \phi}{\partial x} dy + \left(\frac{\partial \phi}{\partial t} - \Lambda \frac{\partial \phi}{\partial x} \right) dt \tag{26}$$

Time derivative measured by an observer bound to the frame of the shock

$$\frac{\partial \phi}{\partial t'} = \frac{\partial \phi}{\partial t} - \Lambda \frac{\partial \phi}{\partial x} \tag{27}$$

Time derivative measured by an observer bound to the frame of the shock

$$\frac{D}{Dt} = \frac{\partial}{\partial t} + (u' + \Lambda) \frac{\partial}{\partial x} = \frac{\partial}{\partial t} + u \frac{\partial}{\partial x} \tag{28}$$

B. Solution of the algebraic system

Let the solution vector and the residual be partitioned as follows:

$$\boldsymbol{Q} = \begin{bmatrix} \boldsymbol{Q}_B \\ \boldsymbol{Q}_T \end{bmatrix}, \ \boldsymbol{R} = \begin{bmatrix} \boldsymbol{R}_B \\ \boldsymbol{R}_T \end{bmatrix} \tag{29}$$

Where:

$$\boldsymbol{Q}_B, \boldsymbol{R}_B \in \mathbb{R}^{\mathcal{T} \times \mathcal{N} \times (\mathcal{M}+1)}, \ \boldsymbol{Q}_T, \boldsymbol{R}_T \in \mathbb{R}^{\mathcal{T} \times (\mathcal{M}+1)} \tag{30}$$

Let the Jacobian of the residual be:

$$\boldsymbol{A} = \begin{bmatrix} \frac{\partial \boldsymbol{R}_B}{\partial \boldsymbol{Q}_B} & \frac{\partial \boldsymbol{R}_B}{\partial \boldsymbol{Q}_T} \\ \frac{\partial \boldsymbol{R}_T}{\partial \boldsymbol{Q}_B} & \frac{\partial \boldsymbol{R}_T}{\partial \boldsymbol{Q}_T} \end{bmatrix} = \begin{bmatrix} \boldsymbol{A}_{BB} & \boldsymbol{A}_{BT} \\ \boldsymbol{A}_{TB} & \boldsymbol{A}_{TT} \end{bmatrix} \tag{31}$$

The solution vector is obtained via Newton iterations with:

$$\boldsymbol{Q} \rightarrow \boldsymbol{Q} - \tilde{\boldsymbol{A}}^{-1} \boldsymbol{R} \tag{32}$$

$\tilde{\boldsymbol{A}}^{-1}$ is an approximation of A^{-1} constructed via Gauss-Seidel iterations.

$$\boldsymbol{X}_B \rightarrow \boldsymbol{X'}_B = \boldsymbol{X}_B + \boldsymbol{A}_{BB}^{-1} (\boldsymbol{R}_B - \boldsymbol{A}_{BB} \boldsymbol{X}_B - \boldsymbol{A}_{BT} \boldsymbol{X}_T) \tag{33}$$
$$\boldsymbol{X}_T \rightarrow \boldsymbol{X'}_T = \boldsymbol{X}_T + \omega \boldsymbol{A}_{TT}^{-1} (\boldsymbol{R}_T - \boldsymbol{A}_{TB} \boldsymbol{X}_B - \boldsymbol{A}_{TT} \boldsymbol{X}_T) \tag{34}$$

$\omega < 1$ is a relaxation factor.

References

[1] Mirels, H., "Test Time in Low-Pressure Shock Tubes," *Physics of Fluids*, Vol. 6, No. 9, 1963, p. 1201. https://doi.org/10.1063/1.1706887.

[2] Cruden, B. A., and Brandis, A. M., "Measurement of Radiative Nonequilibrium for Air Shocks Between 7 and 9 km/s," *Journal of Thermophysics and Heat Transfer*, Vol. 34, No. 1, 2020, pp. 154–180. https://doi.org/10.2514/1.T5735.

[3] Collen, P. L., "Development of a high-enthalpy ground test facility for shock-layer radiation," PhD Thesis, University of Oxford, 2021.

[4] Mirels, H., "Flow Nonuniformity in Shock Tubes Operating at Maximum Test Times," *Physics of Fluids*, Vol. 9, No. 10, 1966, p. 1907. https://doi.org/10.1063/1.1761542.

[5] Morgan, R., and Gildfind, D., "Shock tube simulation of low Mach number blast waves," *International symposium on shock waves*, Springer, 2013, pp. 83–88.

[6] White, D. R., "Influence of diaphragm opening time on shock-tube flows," *Journal of Fluid Mechanics*, Vol. 4, No. 6, 1958, pp. 585–599. https://doi.org/10.1017/S0022112058000677.

[7] Kotov, D. V., Yee, H., Panesi, M., Prabhu, D. K., and Wray, A. A., "Computational challenges for simulations related to the NASA electric arc shock tube (EAST) experiments," *Journal of Computational Physics*, Vol. 269, 2014, pp. 215–233. https://doi.org/10.1016/j.jcp.2014.03.021.

[8] Chandel, D., Nompelis, I., and Candler, G. V., "Computations of High Enthalpy Shock-waves in Electric Arc Shock-Tube (EAST) at NASA Ames," *2018 AIAA Aerospace Sciences Meeting*, American Institute of Aeronautics and Astronautics, Kissimmee, Florida, 2018. https://doi.org/10.2514/6.2018-1722.

[9] Jacobs, P., Gollan, R., Potter, D., Zander, F., Gildfind, D., Blyton, P., Chan, W., and Doherty, L., "Estimation of high-enthalpy flow conditions for simple shock and expansion processes using the ESTCj program and library," 2014. Publisher: Citeseer.

[10] McBride, B. J., *Computer program for calculation of complex chemical equilibrium compositions and applications*, Vol. 2, NASA Lewis Research Center, 1996.

[11] James, C. M., Gildfind, D. E., Lewis, S. W., Morgan, R. G., and Zander, F., "Implementation of a state-to-state analytical framework for the calculation of expansion tube flow properties," *Shock Waves*, Vol. 28, No. 2, 2018, pp. 349–377. https://doi.org/10.1007/s00193-017-0763-3.

[12] Jacobs, P. A., "Quasi-one-dimensional modeling of a free-piston shock tunnel," *AIAA Journal*, Vol. 32, No. 1, 1994, pp. 137–145. https://doi.org/10.2514/3.11961.

[13] McGilvray, M., Austin, J. M., Sharma, M., Jacobs, P. A., and Morgan, R. G., "Diagnostic modelling of an expansion tube operating condition," *Shock Waves*, Vol. 19, No. 1, 2009, pp. 59–66. https://doi.org/10.1007/s00193-009-0187-9.

[14] Gildfind, D. E., Jacobs, P. A., Morgan, R. G., Chan, W. Y. K., and Gollan, R. J., "Scramjet test flow reconstruction for a large-scale expansion tube, Part 1: quasi-one-dimensional modelling," *Shock Waves*, Vol. 28, No. 4, 2018, pp. 877–897. https://doi.org/10.1007/s00193-017-0785-x.

[15] Gollan, R., and Jacobs, P., "About the formulation, verification and validation of the hypersonic flow solver Eilmer," *International Journal for Numerical Methods in Fluids*, Vol. 73, No. 1, 2013, pp. 19–57. https://doi.org/10.1002/fld.3790.

[16] Candler, G. V., Johnson, H. B., Nompelis, I., Gidzak, V. M., Subbareddy, P. K., and Barnhardt, M., "Development of the US3D Code for Advanced Compressible and Reacting Flow Simulations," *53rd AIAA Aerospace Sciences Meeting*, American Institute of Aeronautics and Astronautics, Kissimmee, Florida, 2015. https://doi.org/10.2514/6.2015-1893.

[17] Gollan, R., "POSHAX: Computing post-shock thermochemically relaxing flow behind a steady normal shock," *Division of Mechanical Engineering Report*, Vol. 9, 2007.

[18] Gollan, R., "Computational modelling of high-temperature gas effects with application to hypersonic flows," Ph.D. thesis, 2008.

[19] Glenn, A. B., Collen, P. L., and McGilvray, M., "Experimental Non-Equilibrium Radiation Measurements for Low-Earth Orbit Return," *AIAA SCITECH 2022 Forum*, American Institute of Aeronautics and Astronautics, San Diego, CA & Virtual, 2022. https://doi.org/10.2514/6.2022-2154.

[20] Potter, D. F., "Modelling of radiating shock layers for atmospheric entry at Earth and Mars," Ph.D. thesis, 2011.

[21] Collen, P. L., Satchell, M., Di Mare, L., and McGilvray, M., "The influence of shock speed variation on radiation and thermochemistry experiments in shock tubes," *Journal of Fluid Mechanics*, Vol. 948, 2022, p. A51. https://doi.org/10.1017/jfm.2022.727.

[22] Clarke, J., Di Mare, L., and McGilvray, M., "Spatial Transformations for Reacting Gas Shock Tube Experiments," *AIAA Journal*, 2023, pp. 1–10. https://doi.org/10.2514/1.J062604.

[23] Collen, P. L., Di Mare, L., McGilvray, M., and Satchell, M., "Analysis of Shock Deceleration Effects in the NASA Electric Arc Shock Tube," *Journal of Thermophysics and Heat Transfer*, Vol. 37, No. 2, 2023, pp. 503–512. https://doi.org/10.2514/1.T6619.

[24] Satchell, M., McGilvray, M., and Di Mare, L., "Analytical method of evaluating nonuniformities in shock tube flows: Theory and development," *AIAA Journal*, Vol. 60, No. 2, 2022, pp. 654–668. Publisher: American Institute of Aeronautics and Astronautics.

[25] Satchell, M., Glenn, A., Collen, P., Penty-Geraets, R., McGilvray, M., and Di Mare, L., "Analytical method of evaluating nonuniformities in shock tube flows: Application," *AIAA Journal*, Vol. 60, No. 2, 2022, pp. 669–676. Publisher: American Institute of Aeronautics and Astronautics.

[26] Satchell, M., Di Mare, L., and McGilvray, M., "Flow Nonuniformities Behind Accelerating and Decelerating Shock Waves in Shock Tubes," *AIAA Journal*, Vol. 60, No. 3, 2022, pp. 1537–1548. https://doi.org/10.2514/1.J060375.

[27] Jacobs, P. A., "Shock tube modelling with L1d," 1998.

[28] Clarke, J., Collen, P. L., McGilvray, M., and Di Mare, L., "Numerical Simulation of a Shock Tube in Thermochemical Non-Equilibrium," *AIAA SciTech 2023 Forum*, American Institute of Aeronautics and Astronautics, National Harbor, MD & Online, 2023. https://doi.org/10.2514/6.2023-1797.

[29] Gibbons, N. N., Damm, K. A., Jacobs, P. A., and Gollan, R. J., "Eilmer: an Open-Source Multi-Physics Hypersonic Flow Solver," *Computer Physics Communications*, Vol. 282, 2023, p. 108551. https://doi.org/10.1016/j.cpc.2022.108551, arXiv:2206.01386 [cs].

[30] Satchell, M., Collen, P., McGilvray, M., and Di Mare, L., "Numerical Simulation of Shock Tubes Using Shock Tracking in an Overset Formulation," *AIAA Journal*, Vol. 59, No. 6, 2021, pp. 2102–2112. https://doi.org/10.2514/1.J059829.